



Cell cycle–dependent active stress drives epithelia remodeling

John Devany^a, Daniel M. Sussman^{b,c}, Takaki Yamamoto^d, M. Lisa Manning^b, and Margaret L. Gardel^{a,e,1}

^aDepartment of Physics, Institute for Biophysical Dynamics, James Franck Institute, University of Chicago, Chicago, IL 60637; ^bDepartment of Physics, BioInspired Institute, Syracuse University, Syracuse, NY 13244; ^cDepartment of Physics, Emory University, Atlanta, GA 30322; ^dNonequilibrium Physics of Living Matter RIKEN Hakubi Research Team, RIKEN Center for Biosystems Dynamics Research, Kobe 650-0047, Japan; and ^ePritzker School of Molecular Engineering, University of Chicago, Chicago, IL 60637

Edited by David A. Weitz, Harvard University, Cambridge, MA, and approved January 24, 2021 (received for review October 11, 2019)

Epithelia have distinct cellular architectures which are established in development, reestablished after wounding, and maintained during tissue homeostasis despite cell turnover and mechanical perturbations. In turn, cell shape also controls tissue function as a regulator of cell differentiation, proliferation, and motility. Here, we investigate cell shape changes in a model epithelial monolayer. After the onset of confluence, cells continue to proliferate and change shape over time, eventually leading to a final architecture characterized by arrested motion and more regular cell shapes. Such monolayer remodeling is robust, with qualitatively similar evolution in cell shape and dynamics observed across disparate perturbations. Here, we quantify differences in monolayer remodeling guided by the active vertex model to identify underlying order parameters controlling epithelial architecture. When monolayers are formed atop an extracellular matrix with varied stiffness, we find the cell density at which motion arrests varies significantly, but the cell shape remains constant, consistent with the onset of tissue rigidity. In contrast, pharmacological perturbations can significantly alter the cell shape at which tissue dynamics are arrested, consistent with varied amounts of active stress within the tissue. Across all experimental conditions, the final cell shape is well correlated to the cell proliferation rate, and cell cycle inhibition immediately arrests cell motility. Finally, we demonstrate cell cycle variation in junctional tension as a source of active stress within the monolayer. Thus, the architecture and mechanics of epithelial tissue can arise from an interplay between cell mechanics and stresses arising from cell cycle dynamics.

epithelial tissue | cell mechanics | cell cycle | vertex model

Cells in epithelial tissues adopt a variety of distinct morphologies which are defined during development and maintained throughout the lifetime of an organism (1). Cellular shape and geometry can be perturbed by stretching or wounding, but individual cells within the tissue return to their original shape through increased cellular motility, junctional turnover, neighbor exchange, and proliferation (2–4). In turn, tissue architecture impacts cell fate and tissue physiology (5, 6). Cell division has been implicated as a potential mechanism to regulate monolayer topology (2, 7–10). However, tissue architecture can also change as a result of motion, neighbor exchanges, and shape changes of individual cells in the absence of cell division (11–14). One promising physical framework for predicting collective cell behavior is vertex models which represent confluent epithelial monolayers by a mechanical network of cell–cell junctions (8, 15–18). From these approaches, mechanical descriptions of epithelial tissue dynamics are being developed (15, 19), but key questions remain.

For instance, it remains unclear what processes set the length scale over which cells in a tissue can move or migrate. This length scale helps determine developmental outcomes such as whether convergent extension is effective at generating large-scale changes to the body shape as well as disease outcomes such as whether cells leave a cancer tumor in invasive streams (20, 21). In traditional materials composed of atoms or molecules, particles can freely diffuse when the material is fluid like, but their motion is

arrested in solids when surrounding particles inhibit their mobility. In the context of biological tissues, it is tempting to speculate that the arrest of motion in a dense collection of cells occurs as the system becomes jammed, or solid like, which can arise from changes to either density (22, 23) or cell mechanical properties (24–26). However, there is a third possible mechanism for arrest of motion: the particles in a fluid-like material could also stop moving if the source of fluctuations becomes very small, despite remaining in a mechanically unstable configuration. Fluctuations in biological tissues are driven by active cellular processes such as cell migration, cytoskeletal contraction, and cell division (27–29). Therefore, the scale of fluctuations in a tissue may be regulated in response to extracellular or intracellular cues to control the degree of tissue remodeling.

In model epithelial tissues, it has been observed that the cells are initially more dynamic—changing neighbors and moving significant distances—and at later times that motion arrests (5, 30–34). Because these changes occur with minimal genetic or biochemical gradients, such epithelial monolayers are an ideal system to study whether cell arrest is governed by an underlying rigidity transition (e.g., collective solidification) caused by changes in density or cell mechanics or instead by a decrease in active stress fluctuations in a material that remains fluid like. Particle-based models for tissues predict decreased cell motion arising from reduced interstitial space at increased cell density (12, 22, 23, 35). In contrast, vertex models predict that the cell density is not a direct control parameter for cell dynamics (24). Instead, vertex models predict that observed steady-state cell shape, tuned by varying passive cell mechanics and active forces, is the control parameter for cell motility (8, 17, 19, 24, 25). Cell shape, density, and cell adhesion have all been implicated in the arrest of cell motion in epithelial monolayers (5, 30, 31, 33). Furthermore,

Significance

The morphology of biological tissue is determined by the shape and density of constituent cells. Here, we measure the dynamics of cells in model epithelial tissues to study the evolution of their shape and density over time. Guided by a mathematical model, we find that cell shape is controlled by rigidity and active stresses within the tissue. We then show that cell cycle dynamics are the source of active stress that drives epithelial remodeling.

Author contributions: J.D., D.M.S., M.L.M., and M.L.G. designed research; J.D., D.M.S., and T.Y. performed research; J.D., D.M.S., T.Y., M.L.M., and M.L.G. contributed new reagents/analytic tools; J.D. and D.M.S. analyzed data; and J.D., D.M.S., T.Y., M.L.M., and M.L.G. wrote the paper.

The authors declare no competing interest.

This article is a PNAS Direct Submission.

Published under the PNAS license.

¹To whom correspondence may be addressed. Email: gardel@uchicago.edu.

This article contains supporting information online at <https://www.pnas.org/lookup/suppl/doi:10.1073/pnas.1917853118/-DCSupplemental>.

Published March 1, 2021.

changes to cell density also regulate signaling pathways that could influence single-cell mechanics and cell–cell interactions (36), and cell divisions also introduce active stress fluctuations, which in turn affect cell shape (24, 28, 37–39). Thus, it remains unclear how cell density, cell mechanics, and active stress fluctuations contribute to the regulation of epithelial monolayer remodeling dynamics.

Here, we use epithelial monolayer remodeling as a model system to investigate the biophysical regulation of epithelial architecture and dynamics. After forming a confluent monolayer, cells continue to divide and change shape over time until reaching a final state characterized by low motility and more regular cell shapes. Such monolayer remodeling is robustly observed, with qualitatively similar evolution in cell shape and dynamics over a large range of experimental conditions. To tease apart the effects of cell density changes from other mechanical perturbations, we study monolayers formed atop an extracellular matrix (ECM) with varied stiffness. This variation in substrate stiffness causes the cell densities to change significantly, but we find relatively little correlation between density and cell motion. In contrast, we find a striking data collapse when cell velocities are plotted as a function of observed cell shape, as predicted by active vertex models. To understand whether observed cell shapes are primarily regulated by active fluctuations or by changes to single-cell mechanical properties, we perturb the monolayer with pharmacological interventions that interfere with cell proliferation and the cytoskeleton. We find that inhibition of the cell cycle immediately arrests cell motion and shape change, suggesting that cell cycle–dependent active stress contributes significantly to monolayer dynamics and remodeling. Moreover, across all experimental conditions we find that the average cell shape in the homeostatic final state is well correlated with the cell division rate, suggesting that suppressing cell cycle–based fluctuations leads to an arrest of cell motion that is independent of the underlying cell mechanics. Finally, we show that cell cycle–dependent changes in junctional tension are an important source of active stress in the tissue and use simulations to demonstrate the different tissue architectures that can be realized by modeling cell cycle–dependent changes in edge tensions. Together our results demonstrate that cell geometry and cell cycle dynamics control cell shape remodeling in epithelial monolayers.

Results

Remodeling of Confluent MDCK Monolayers to Achieve Homeostatic Architecture. To measure the shape and speed of individual cells in a simple epithelial monolayer, we created an MDCK cell line that stably expresses green fluorescent protein localized to the plasma membrane via the transmembrane protein stargazin. We seeded these cells at high density on collagen I gels and imaged multiple fields of view using time-lapse fluorescence microscopy. Initially, the monolayer was not continuous, and there were numerous cell-free voids (Fig. 1A). Over time, the cells closed gaps to form a continuous monolayer spanning ~15 mm; we designate this as $t = 0$ (Fig. 1A). Over the following 12 h, the cells within the monolayer change shape until a steady-state geometry and density is achieved (Fig. 1A, $t = 720$ min, [Movie S1](#)). Thus, we use this as a model system to study epithelial tissue homeostasis by which cell shape and density is recovered after injury through wound healing and monolayer remodeling (Fig. 1B). While previous work has focused on mechanisms of collective migration in wound healing (40–42), here we focus on the process by which the cells within a confluent monolayer change shape over time.

We use image segmentation to extract cell shape, size, and positions over time ([Materials and Methods](#) and [Movie S1](#)). To quantify cell shape, we use cell vertex locations to reconstruct a polygon with a well-defined perimeter p and area A to calculate the shape parameter (area-normalized perimeter) $q = p/A^{1/2}$; this quantity is bounded from below by objects with a circular shape ($q_{\text{circle}} \approx 3.54$), and most cells are observed to have a shape

parameter greater than that of a regular hexagon ($q_{\text{hexagon}} \approx 3.72$) ([SI Appendix, Fig. S1](#)) (24, 25).

We observe cell shape remodeling, along with changes in density and speed, takes place for ~12 h until the system arrests. These dynamics are not sensitive to the details of how time or spatial averaging is performed ([SI Appendix, Figs. S2 and S3](#)). We also confirmed they are independent of initial seeding density ([SI Appendix, Fig. S4](#)), consistent with previous data (31). Similarly to prior observations (30, 34), cell speed decreases (Fig. 1C–E and [SI Appendix, Fig. S2B](#)) as the density increases from cell proliferation (Fig. 1F). However, we also observe changes in cell shape over time (Fig. 1G). This reduction in shape parameter is correlated with reduced motility in models and experiments where there is no change in density (5, 19, 32). Therefore, from these data alone, the order parameters controlling the steady-state cell shape and density in epithelial tissues are impossible to discern.

Cell Shape and Speed Are Correlated in Active Vertex Models. To further understand the process of monolayer remodeling, we explore predictions of a thermal Voronoi model (43, 44). This model is a variation of standard vertex models which incorporates a simple Brownian noise on each cell to account for active mechanical stress applied by the cells. This model has two key parameters (Fig. 2A): a temperature T that represents via uncorrelated noise the magnitude of active stress fluctuations acting on each cell and a parameter p_0 that represents the target perimeter of each cell and encodes the mechanical properties of a cell, including cell–cell adhesion and tension in the cortically enriched cytoskeleton. In steady state, these two parameters give rise to a predicted observed shape parameter and cell mobility (19, 44). Importantly, in isotropic tissues, a shape parameter of ~3.8 reflects the onset of rigidity in the vertex model, whereby higher shape parameters reflect a more fluid-like tissue (19, 24, 25), although the exact location of the transition point depends on the degree of cell packing disorder (45, 46). We expect that the cells tune their active fluctuations and mechanical properties during monolayer remodeling, resulting in potentially time-dependent parameters $T(t)$ and $p_0(t)$ and different “trajectories” through model parameter space (Fig. 2B and [SI Appendix, Fig. S5A](#)). Along these parameter trajectories we measure the resulting steady-state shape and speed of cells in simulations (Fig. 2C and [SI Appendix, Fig. S5B](#)) which then can be compared to the experimental measurements.

We find that substantially different trajectories through model parameter space can generate similar curves in a plot of typical cell displacements versus observed cell shape, as shown by all of the solid lines in Fig. 2B and C. This is a restatement of the result that in vertex models, observed cell shape and cell motility are highly correlated (5, 19). In our experiments, we observe a similar relationship between shape and speed resembling these model trajectories (Fig. 2D), suggesting that vertex models may be able to predict features of remodeling in proliferating epithelial layers. Fig. 2B and C also highlights that there is an important exception: the observed shape–motility correlation and convergence breaks down when the temperature (i.e., active stress fluctuation) drops to zero, while the cell mechanical stiffness encoded by p_0 is still in the floppy regime with $p_0 \gtrsim 3.8$ (see dashed lines in Fig. 2B). In this case, the “zero temperature” system stops moving, even though the underlying mechanics of the layer are floppy and weak. Since in the real monolayers, active stress is generated by cellular processes, we explore these ideas further by considering how monolayer remodeling is impacted by perturbations to extracellular or intracellular pathways.

Monolayer Remodeling Is Regulated by Matrix Stiffness and Signaling Pathways. The stiffness of the ECM can alter cell migration rates through effects on focal adhesion dynamics and cell spreading (47). To explore how epithelial tissues are impacted by the

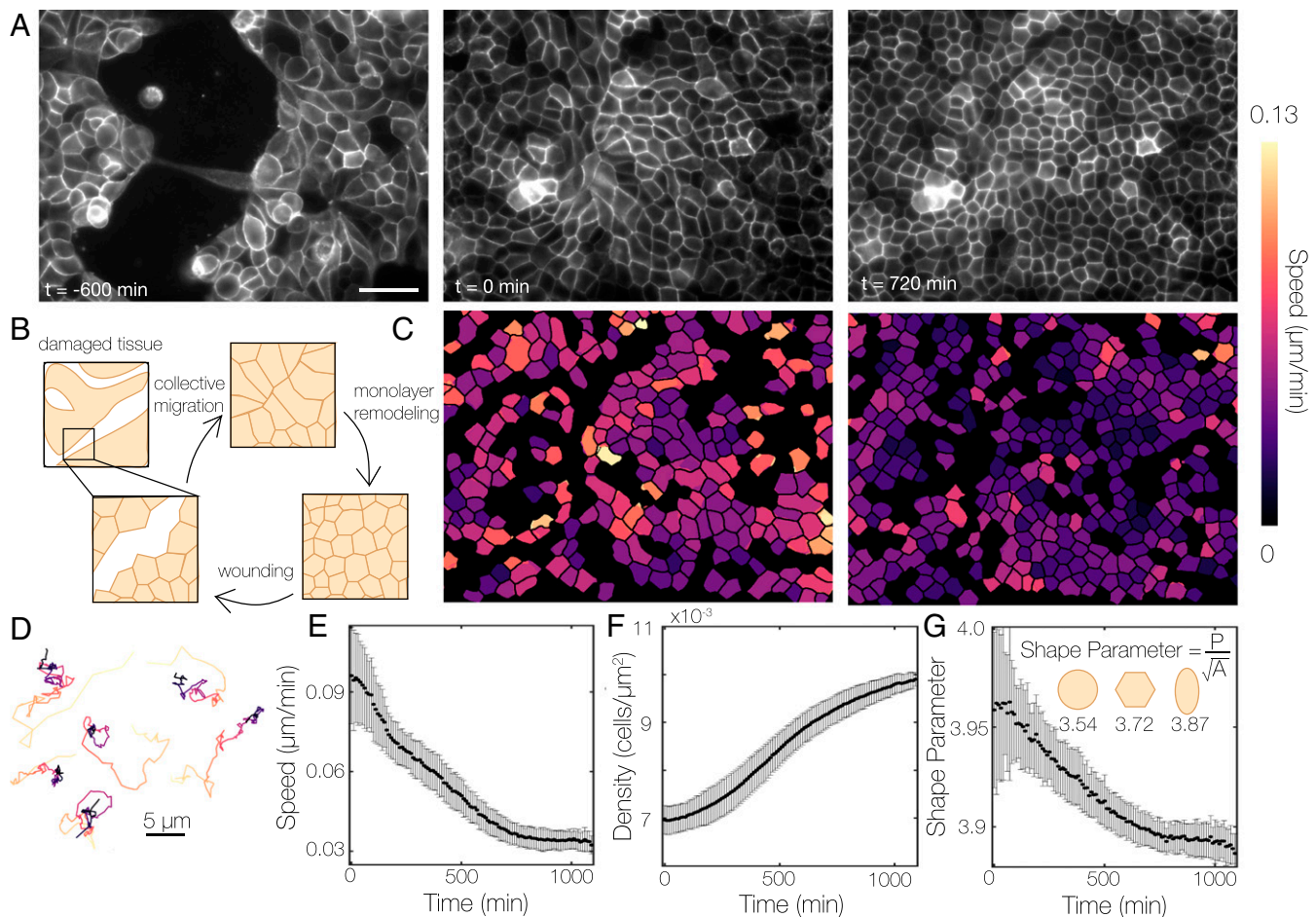


Fig. 1. Cell shape remodeling leads to homeostatic monolayer architecture. (A) Cells were plated on collagen gel substrates at $t = -1,000$ min. By $t = -600$ min, cells have aggregated into large colonies which collectively migrate to fill open space. At $t = 0$ min, cells have formed a confluent monolayer. Over the next 720 min, cells become denser and cell morphology becomes increasingly regular. (Scale bar, 50 microns.) (B) Schematic of the process observed in A. A tissue may be wounded, resulting in collective migration followed by monolayer remodeling to the normal epithelial architecture. (C) Heat map of single cell speeds plotted over the segmented cell outlines from images shown in A. Areas in black contain cells which were ignored due to potential segmentation errors. (D) Randomly selected cell trajectories from $t = 0$ to $t = 1,100$ min; color indicates time. (E–G) Sample averaged values of speed, density, and cell shape at each time point across 60 fields of view in the sample depicted in A. Error bars represent SD between fields of view.

physical properties of the ECM, we varied the underlying collagen gel stiffness and density by either increasing the concentration of collagen or crosslinking gels with glutaraldehyde (48). This produced gels with Young's moduli ranging from ~ 200 to 2,000 Pa (49). On all gels, qualitatively similar dynamics in cell shape, motion, and density are observed during monolayer remodeling

(SI Appendix, Fig. S6), but there are quantitative differences. For instance, at the onset of confluence when the cell speeds are large ($0.07 \mu\text{m}/\text{min}$), the cell density is $\sim 50\%$ lower on the stiffer ECM conditions than the soft ones (Fig. 3 A and B and Movie S2). These differences remain as the density increases and cell speed decreases during monolayer remodeling (Fig. 3 A and B). Thus,

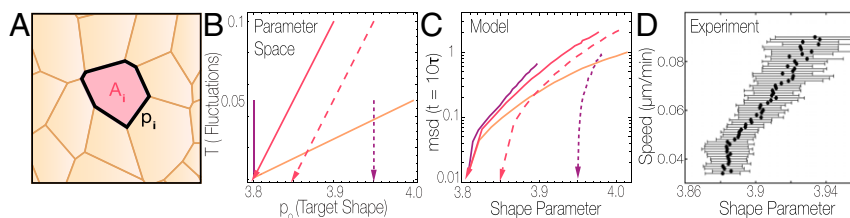


Fig. 2. Active vertex models predict a relationship between cell shape and speed during monolayer remodeling. (A) Schematic of the thermal Voronoi model, in which each cell has a target geometry specified by a preferred perimeter p_0 and area A_0 . Each cell is subject to Brownian noise with amplitude set by the temperature T . (B) Parameters of the thermal Voronoi model were varied along several representative curves. Along these curves, a simulated monolayer was equilibrated at each point, after which measurements were made on the monolayer. Solid curves approach $T = 0$ at a value of p_0 in which the tissue is weakly rigid, while dashed curves approach $T = 0$ at a value of p_0 in which the tissue is floppy. Colors represent trajectories with different slopes. (C) Observed values of speed and cell shape. Line styles correspond to the equivalent parameter space trajectories shown in panel B. mean squared displacement (MSD) is given in units of $\sqrt{\text{Cell Area}}$ over a time window of 10 natural time units. Data are ensemble averages of 30 simulations each with $n = 1,000$ cells. (D) Experimental relationship between cell shape and speed measured for WT dataset on 2 mg/mL collagen matrix.

across different matrix stiffness, the number density at which cell speed reaches its minimal value varies substantially (Fig. 3B). This is a strong indication that number density is not directly controlling the arrest of cell motion.

In contrast, the cell shapes robustly and reproducibly change during monolayer remodeling, with the arrest of cell motion occurring at a consistent shape parameter of 3.88 (Fig. 3C). Because our collagen gels only span a small range of stiffness, we performed similar experiments on stiffer polyacrylamide gels (16 kPa) and glass and observed similar results, suggesting that this behavior is independent of substrate stiffness across a large range (SI Appendix, Fig. S7). Therefore, cell shape appears to be a robust parameter to predict dynamics and structure of monolayers formed atop different ECM stiffness, in agreement with vertex model simulations.

As demonstrated in the simulation results in Fig. 2B and C, these shape–velocity curves do not by themselves shed light on whether the arrested motion arises predominantly from changes in tissue mechanics or the magnitude of active stresses. An important exception is in regimes where the active fluctuations are driven toward zero while the underlying cell mechanics remains floppy—this scenario results in distinctly different paths through shape–velocity space (dashed lines in Fig. 2C).

To access different regimes of tissue mechanics and active stress generation, we performed a screen of pharmacological perturbations to cell signaling by treatments that altered focal adhesion, cell cycle, and Rho GTPase signaling (Movies S3 and S4). Across all conditions, we observe qualitatively similar monolayer remodeling dynamics that result in arrested cell motion with a characteristic cell shape and density (SI Appendix, Figs. S6 and S8). However, there are substantial quantitative changes that contrast with those found in Fig. 3. To illustrate, we consider the impact of fibroblast-secreted growth factors by forming monolayers in fibroblast-conditioned medium (FCM). We observe that the cell shapes in FCM-treated monolayers are more elongated, with a higher shape parameter, throughout the experiment (Fig. 4A and Movie S4). At the onset of cell motion arrest, the shape parameter is >3.94 , a value much higher than the observed shape in control cells even many hours before arrest (Fig. 4B). This results in significantly higher values of shape parameters throughout monolayer remodeling (Fig. 4B). Across these perturbations, we consistently observe a correlation between the changes in shape parameter and cell speed but observe significant variations in the

final shape parameters that occur at cell motion arrest (SI Appendix, Figs. S8 and S9).

Cell Division Rates Control Cell Shape Remodeling. The diversity of monolayer architectures observed across all conditions is demonstrated by plotting the final shape parameters and density (Fig. 5A). With these perturbations, the steady-state architecture varies twofold in density, with cell shapes ranging from elongated to compact, but with no clear correlation between density and shape (Fig. 5A). However, many perturbations reduced the rate of cell divisions (SI Appendix, Fig. S6B). Plotting the final cell shape as a function of the cell division rate for all conditions reveals an inverse correlation (Fig. 5B). Monolayer remodeling obtained from another common epithelial model, CACO-2 cells, with a much lower cell division rate, can be overlaid on this data (Fig. 5B and SI Appendix, Fig. S8).

To explore how cell division impacts monolayer architecture, we first consider the direct consequences of cell division (9, 10). From purely geometric considerations, one would expect a local reduction in cell shape parameter as a result of topology and aspect ratio changes after a division (8, 9). Further, oriented cell divisions can directly change cell shape by producing two daughter cells with lower aspect ratio (2, 50). To access the contribution of division to the overall shape change, we analyzed shape change in individual cells in our segmentation data. We measured the shape changes of a dividing cell and its immediate neighbors before and after division, which we classify into three groups based on their contact relationship with the daughter cells (Fig. 5C). Similar to previous findings (2, 7, 50), we observe a strong alignment of cell division along the long axis (Fig. 5C and D). The division results in a reduction of the aspect ratio of the dividing cell but, on average, modestly increases the shape parameter (Fig. 5E, Group 1). Furthermore, there is minimal change in the aspect ratio or shape parameter for neighboring groups of cells (Fig. 5E, Groups 2 and 3). Considering the weighted average of all groups, the impact of cell division on shape parameter changes is negligible (Fig. 5E, weighted average). By tracking shape changes occurring in individual cells throughout interphase, we further verified that the direct effects of cell division are small compared to shape changes occurring through changes in cell junction length in nondividing cells (SI Appendix, Figs. S10 and S11). Thus, local distortions and topological changes during cell division alone are insufficient to explain the contribution of cell division rate to monolayer remodeling.

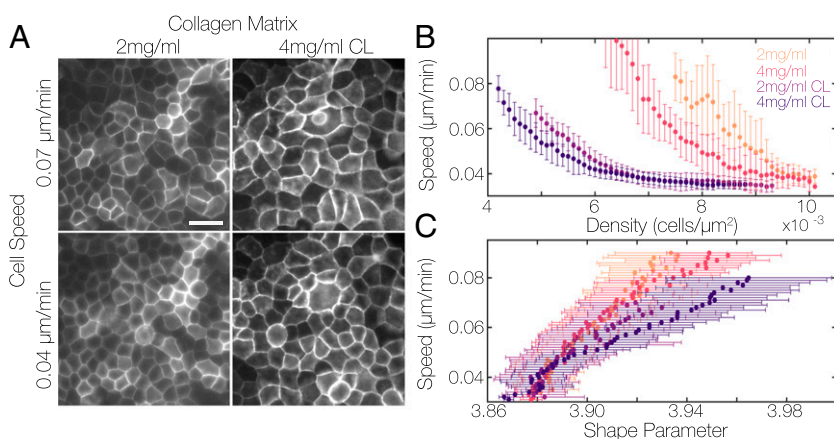


Fig. 3. Monolayer remodeling is independent of cell density across perturbations to substrate stiffness. (A) Images of monolayers remodeling on substrates with different stiffness near the beginning and end of the experiment. CL is glutaraldehyde crosslinked collagen gel. (Scale bar, 25 microns.) (B) Correlation between cell speed and cell density for monolayers on substrates of different stiffness. (C) Correlation between cell speed and shape parameter for monolayers on different substrates. Quantities are averaged over a field of view containing at least several hundred cells for each time point, and then field of view measurements are binned together by speed in 0.001 increments. Error bars represent the SD of each bin.

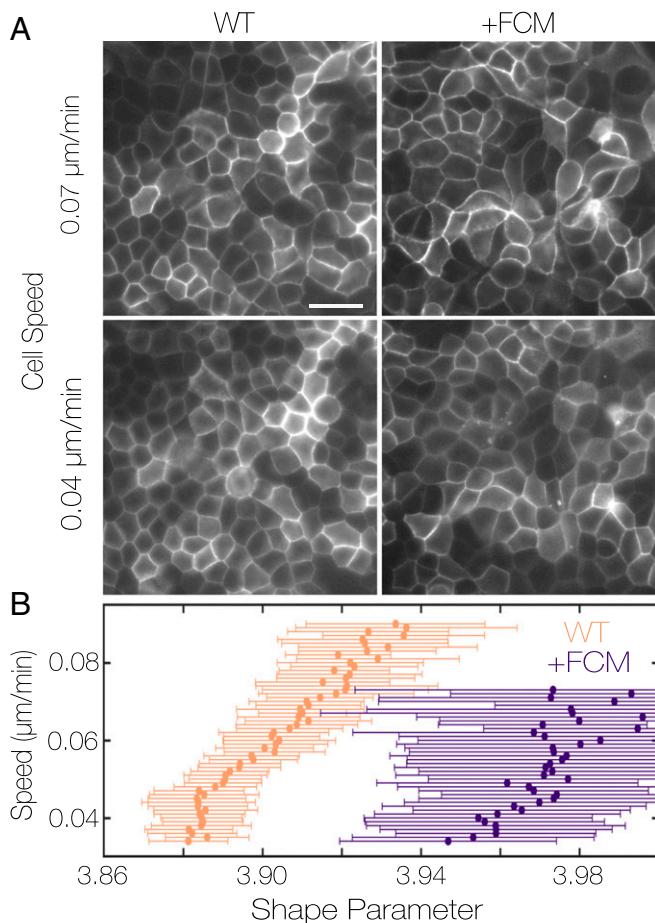


Fig. 4. Intracellular signaling alters cell shape during monolayer remodeling. (A) Images of monolayers at the beginning and end of a remodeling experiment under WT conditions or treated with 1:1 fibroblast-conditioned medium to culture medium. (Scale bar, 25 microns.) (B) Correlation between speed and density for control and FCM-treated monolayers. Quantities are averaged over a field of view containing at least several hundred cells for each time point, and then field of view measurements are binned together by speed in 0.001 increments. Error bars represent the SD of each bin.

Other sources of active stresses within monolayers include cell motility (19, 24, 41) and junctional remodeling (51, 52). Compared to other experiments (e.g., wound healing) which show speeds up to 0.7 μm/min (40), the extent of cell motion in our

experiments is low (<0.1 μm/min). One well-documented type of junctional remodeling that drives cell rearrangements is a T1 transition (8), which we observe in the monolayer (*SI Appendix, Fig. S12*). However, the overall number of cell rearrangements is quite low. Therefore, we surmise that the dominant source of active stresses driving monolayer remodeling is junction length changes in the absence of neighbor exchanges.

Active Stress Originates from CDK1-Dependent Regulation of Cell Mechanics. Our pharmacological screen included many factors known to impact cell migration, adhesion, and force generation including perturbations to RAC, ROCK, FAK, and Integrin signaling pathways. Surprisingly, these perturbations had little impact on the overall motions within the monolayer (*SI Appendix, Fig. S13*). However, we did observe a dramatic and immediate decrease in cell speed upon perfusion of an inhibitor of cyclin dependent kinase 1 (CDK1), which blocks the cell cycle. After initiating a monolayer remodeling experiment, CDK1 inhibitor-containing media was perfused in at $t = 310$ min. We observed a striking reduction in cell motion within 20 min of inhibiting CDK1 (Fig. 6A–C and *Movie S5*). After washing out the inhibitor at $t = 580$ min, there was an immediate recovery of cell motion: remodeling was reinitiated, and the time evolution of changes in cell shape and speed were similar to those initially observed (Fig. 6A–C and *Movie S5*). To quantitatively compare these curves, we shifted the postwashout shape parameter data by rescaling the time to $t - 400$ min; this delay time and rescaling is indicated by dashed lines Fig. 6C and D. Remarkably, with this rescaling, the data evolve in almost quantitative agreement with each other and, moreover, are comparable to the evolution of unperturbed wild-type (WT) monolayers (Fig. 6D). These data are consistent with the hypothesis that CDK1 inhibition dramatically reduces the active stress fluctuations (T, in the model). The enhanced motion observed upon inhibitor removal underscores that tuning cell cycle dynamics may be a means to modulate the active stresses.

As an alternate means to arrest the cell cycle, we used mitomycin C to abrogate DNA replication and observed a similar arrest of monolayer movement (*Movie S6*). Interestingly, inhibition of cell division by low doses of nocodazole does not reduce cell motion significantly (*Movie S7*). Nocodazole allows cells to enter mitosis and initiate mitotic rounding but prevents further progression of mitosis. This is consistent with our data that cell division per se is not the primary source of stress in the monolayer (*SI Appendix, Fig. S11*). Instead, these stresses arise in the interphase portion of the cell cycle. Together with our characterizations of cell shape changes, we surmise these may come from cell cycle-dependent effects on cell mechanics (53, 54).

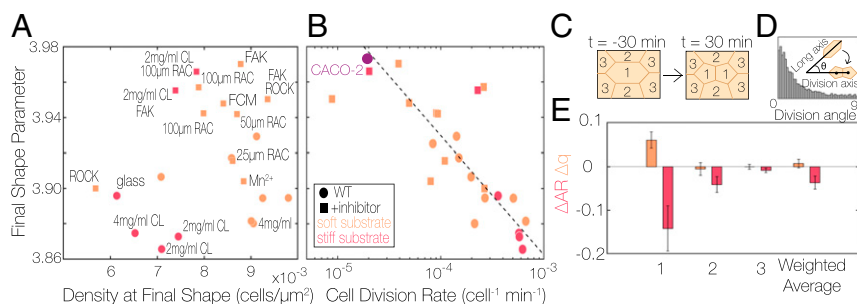


Fig. 5. Cell shape remodeling is dependent on cell division rate. (A) Shape parameter versus density when the monolayer reaches a speed of 0.04 μm/min for all inhibitor conditions tested. (B) Final shape parameter versus the cell division rate from $t = 200$ min to $t = 600$ min for all conditions in A. Logarithmic fit to data are plotted at dashed line. Each data point in A and B are the average of >10 time points after reaching the final shape from >30 fields of view from one experiment. (C) Schematic of cells which may experience direct changes in geometry during cell division; 1 is the dividing cell, 2 is a neighbor of both daughter cells, and 3 is a neighbor of one daughter cell. (D) Histogram of measured angle between the cell's interphase long axis and the division plane during WT experiments ($n = 3,137$ cell divisions). (E) Resulting changes in shape and aspect ratio for the dividing cells and neighbors adjacent to one or both cells are plotted. Error bars represent the SD of three WT experiments on 2 mg/mL collagen each with at least 1,000 cell divisions measured.

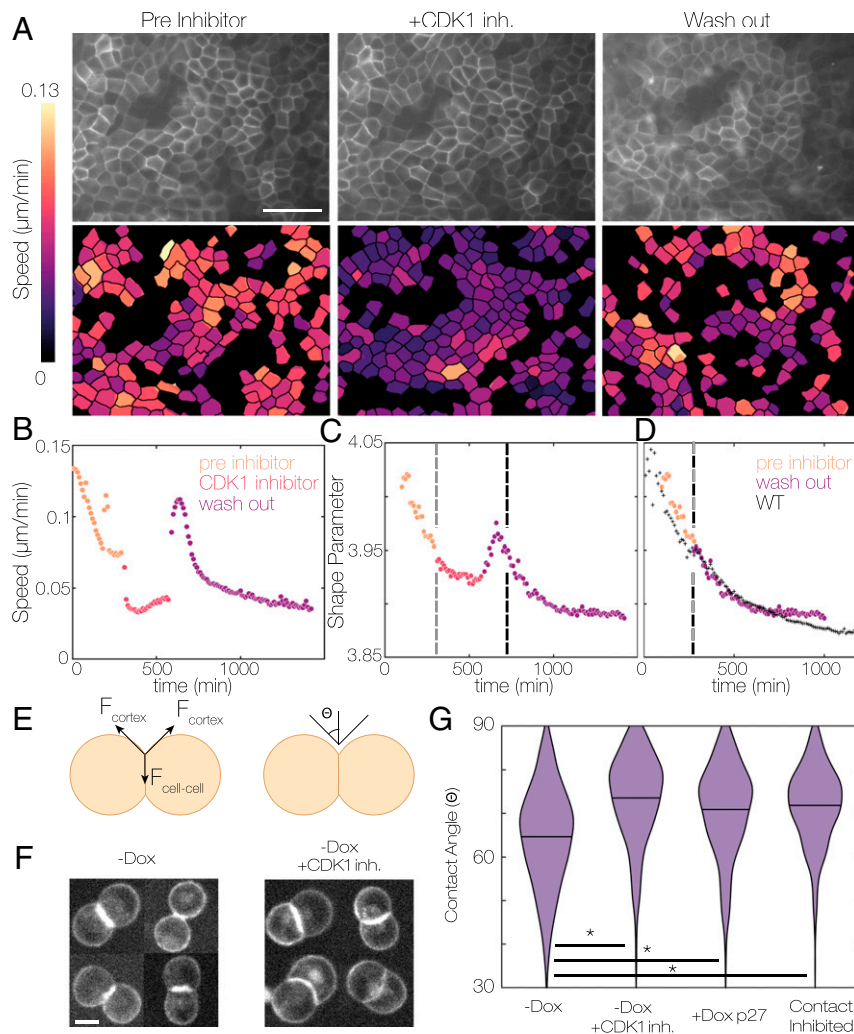


Fig. 6. Cell division is a source of active stress required for monolayer remodeling. (A) Representative field of view of monolayer during CDK1 inhibitor wash in experiment. Below each image, heat maps of cell speed for successfully segmented cells are displayed. Preinhibitor is 30 min before adding the inhibitor. Inhibitor is 30 min after adding the inhibitor. Wash out is 120 min after washing out the inhibitor. (Scale bar, 50 microns.) (B) Average cell speed versus time during CDK1 inhibitor wash in experiment. (C) Average cell shape versus time during CDK1 inhibitor wash in experiments. (D) Time-shifted shape versus time curves comparing WT and CDK1 inhibitor wash in data. CDK1 inhibitor wash in data points represent the time average of 12 fields of view in one sample. WT data represents the average of three independent experiments each with >20 fields of view. CDK1 inhibitor is 5 μM RO-3306. (E) Schematic of cell contact angle measurements. Force balance at the contact gives rise to a contact angle Θ . (F) Representative images of MDCK cell doublets in suspension and in the presence and absence of CDK1 inhibitor 5 μM RO-3306. (Scale bar, 10 μm .) (G) Measurement of MDCK tet-p27 cell contact angles under different conditions. -Dox: cells without doxycycline; +CDK1 inh.: 5 μM RO-3306; +Dox p27: 200 ng/mL doxycycline; and Contact inhibited: cells cultured to high density before resuspension, no doxycycline added. -Dox $n = 512$, -Dox +CDK1 inh. $n = 480$, +Dox p27 $n = 394$, and Contact inhibited $n = 565$. Data come from three experimental replicates. * $P < 0.001$.

To test this, we examined the geometry of cell–cell contacts formed by suspended cell doublets. As demonstrated previously (55), this contact angle Θ can be related to the balance between tension of the cell–cell interface ($F_{\text{cell-cell}}$) and cortex (F_{cortex}) (Fig. 6E). We first measured the contact angle under both WT and CDK1 inhibitor treatment and noticed a significant increase in the cell contact angles when CDK1 was inhibited (Fig. 6G). To explore whether increased cell–cell contact angle is observed with other means of cell cycle arrest, we overexpressed p27^{kip1}, a protein which binds and inactivates cyclin-dependent kinases to arrest the cell cycle, that is expressed during contact inhibition (56). To isolate CDK-dependent effects, we used a variant of the protein which lacks a C-terminal domain known to interact with RhoA (57, 58). Cell pairs overexpressing p27^{kip1} also had increased contact angles compared to WT conditions. Finally, we measured contact angles of cells obtained from dense contact-inhibited

cultures similar to the conditions at the end of monolayer remodeling experiments and observed an increase in contact angle (Fig. 6G). Thus, all of these data demonstrate a cell cycle dependence of the force balance at the cell–cell interface relative to the free cortex. Together with effects of CDK1 inhibition on monolayer remodeling (Fig. 6A–D), these data strongly suggest that cell cycle dependencies in junctional tension are a primary source of active stress that drives monolayer remodeling.

Cell Cycle Arrest Leads to Low-Fluctuation Arrest of Motility in the Monolayer. To capture cell cycle–dependent junctional tension in the vertex model, we built upon previous work that considered the consequences of system-wide fluctuations in interfacial tension (59). Here, we simulate systems in which only a subset of edges, which we term “active edges,” generate fluctuating interfacial tension with a characteristic persistence time scale, τ (Fig. 7A)

(59). At the beginning of these simulations, all edges are active, and the fraction of active edges, ϕ , is reduced from 1 to 0 over the course of a simulation. This emulates the effect of varying the fraction of cell cycle-arrested cells in the monolayer (Fig. 7A). Concretely, we randomly select an active edge every τ^R natural time units and permanently eliminate the fluctuation of the edge. We observe that as ϕ decreases, the average cell speed diminishes (Fig. 7B). Notably, this parametric plot of speed versus active edges is nearly independent of the tissue-stiffness parameter p_0 (Fig. 7B). To compare this to experiments, we used the pip degron Fluorescent Ubiquitin Cell Cycle Indicator (pip-FUCCI) system to directly monitor cell cycle progression during epithelial remodeling (60). Similar to previous results, we see that the fraction of cells in later stages of the cell cycle (S, G2) decreases with time as the cells experience contact inhibition of proliferation (Fig. 7C) (56, 61). When the cell speed is plotted as a function of the fraction of cells which are early in the cell cycle or exited from the cell cycle (G1/G0), we see that an increasing fraction of such cells correlates with a decrease in overall cell motility (Fig. 7D), similar to the simulation results.

To place this simulation data within a broader framework for cell arrest, we plot the speed versus cell shape for $p_0 = 3.7-4.0$. As expected from the homogeneous fluctuation Voronoi model results (Fig. 2), as the fraction of active edges decreases, the speed decreases and the shape parameter approaches p_0 (SI Appendix, Fig. S14). Along these curves, cell motion arrests at a shape parameter approximately equal to the target shape index p_0 , with very little dependence on τ^R . Moreover, the qualitative shapes of these curves over a range of p_0 show little sensitivity to the value of p_0 and resemble the experimental data (Fig. 7E). We conclude

that at later times in experiments, the cell cycle arrests due to contact inhibition. This leads to a reduction of active stress and the monolayer motility arrests in a “low fluctuation” regime (Fig. 7F). This transition to a low fluctuation regime contrasts with the fluid-solid jamming transition (5, 19, 30). In contrast to the presently proposed scenario, in a jamming transition, cell motion would arrest even as large fluctuations in active stresses persist (Fig. 7F). These different scenarios present two distinct paths for controlling cell shape and movement in epithelial tissue.

Discussion

The mechanisms that regulate epithelial architecture are central to understanding tissue morphogenesis in development, maintenance, and disease. While cell proliferation results in direct changes in topology (9, 10), this does not account for the shape remodeling we observe. In recent years, the development of mechanical models of tissue as active soft materials has provided predictive power to relate local cell mobility and shape. The vertex model predicts that cell motion arrests as cell shapes approach a value that is a sharp rigidity transition, independent of cell density (19, 25). Our data of epithelial remodeling atop matrices with varied stiffness are largely consistent with this model. As the remodeling proceeds, there is twofold variation in the monolayer density, but all data collapse on to a “universal” curve of the cell speed as a function of shape parameter. Moreover, the shape parameter at the onset of arrest is 3.88, which is within the range of transition points predicted by vertex models (46). Several previous studies have illustrated the potential of a jamming framework for understanding motion arrest in epithelia (5, 12, 31–33). However, our data systematically challenge model epithelia with perturbations to demonstrate the robustness of the speed-shape parameter

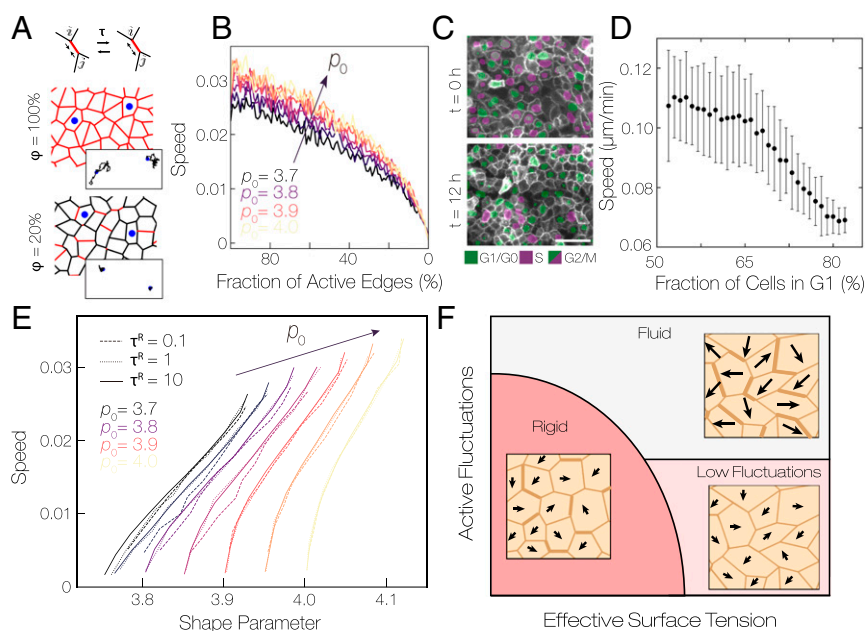


Fig. 7. Active edges as a source of stress in epithelial tissue. (A) Schematic of vertex model with junction tension fluctuations. A fluctuating additional tension is applied between junctions i and j . The fluctuations can be either contractile or extensile and have a characteristic persistence time τ (see SI Appendix for values of all simulation parameters used). Snapshots of cellular configuration at $\phi = 100\%$ and 20% are also shown, respectively ($\tau^R = 1$). (B) Plot of cell speed versus the fraction of active edges in simulated vertex models with fluctuating edge tension ($\tau^R = 1$). Different curves represent different values of the target shape parameter p_0 . (C) Images of MDCK monolayers with cell cycle information extracted from pip-FUCCI biosensor. Images from the individual biosensor channels are segmented and overlaid in pseudocolors green (PIP-Venus) and purple (Geminin-mCherry). Presence of only green indicates G1/G0 phase, only purple indicates S phase, and both markers indicates G2/M phase. (D) Plot of cell speed against fraction of cells in G1/G0 phase of the cell cycle. Error bars represent the SD between 30 fields of view. (E) Plot of cell speed versus shape parameter from simulations. Curves represent different values of τ^R (dashed, dotted lines) and the target shape parameter p_0 (color scale). (F) Schematic phase diagram of epithelial arrest, in which edge thickness represents the magnitude of tension on an edge and arrows represent cell displacements. In addition to fluid and jammed phases which occur at different cell shapes, monolayers can arrest at high average cell shape parameter, indicating a low fluctuation regime. In this low fluctuation regime, the magnitudes of active fluctuations are too small to produce large cell displacements and frequent neighbor rearrangements.

correlation. Importantly, our data strongly support the utility of cell shape, rather than density, as an order parameter to assert the arrest of cell movement and local epithelial tissue mechanics.

Our data from perturbed systems, however, do not show arrested cell motion at a shape at the predicted jamming transition. Across a myriad of pharmacological stimulations and perturbations to signaling pathways, cell motion is arrested even at larger shape parameters and over a wide range of densities. After observing that CDK inhibition immediately arrests the monolayer, we explored the possibility of reducing fluctuations in the monolayer as cells arrest the cell cycle via contact inhibition. In these simulations, the monolayer can be arrested at various cell shapes as the fluctuations are reduced. In these conditions, arrest occurs at cell shape approximately equal to the model target shape parameter p_0 ; observing changes in the shape–speed curves corresponds to changing the underlying mechanical properties of the cells. By exploring predictions of the vertex model simulations, a likely possibility is that the effects of these perturbations on active stress are also coupled to changes in the preferred cell shape. However, it may be that additional active stress–dependent effects on junction remodeling are not captured by our vertex model.

In the fluid regime, the standard vertex model rapidly equilibrates at low temperatures, and, at $T = 0$, the final observed and target shape are the same. In such models, perturbations that affect the final shape of cells result in tissues with vastly different mechanical responses. Specifically, these models predict that tissues that arrest due to jamming with target cell shape parameters close to or below 3.8 would be stiffer and less sensitive to small mechanical perturbations than those that arrest due to a decrease in active stress while remaining floppy, with target cell shape parameters significantly above 3.8. Thus, while previous work attributed the arrest of epithelial monolayers to a rigidity transition dependent on density (30, 34) or mechanics (5, 25, 32), our work suggests that arrest can also occur because of a reduction in active stress. Mechanical measurements of epithelia will be required to probe the energy landscape in detail and understand the differences between these scenarios.

In addition, standard vertex models may be too simple to capture the mechanical response in the limit of small active stresses. Recent experiments suggest the existence of dynamic energy barriers, which may prevent equilibration over experimental time scales, arising from junctional stability (4, 62) and/or remodeling (52). In this scenario, small but finite fluctuations would not be sufficient to cross those dynamic energy barriers, and so the tissue “freezes” into a metastable state. Thus, a reduction of active stresses could quench the tissue into an arrested state of lower, but nonzero, rigidity. Further work is needed to explore how energetic barriers in remodeling can be exploited for control over tissue mechanics.

The epithelial remodeling we observe is primarily driven by individual junctional length changes, with little contribution from neighbor exchanges or cell division. The limited number of neighbor exchanges observed distinguishes this remodeling from the highly fluid-like behavior observed in other scenarios (51, 63). We find that cell cycle regulation is the primary source of active stress driving monolayer remodeling. The wide variation in observed shapes across perturbations can be understood by considering their impact on cell proliferation rate. Perturbations that decrease proliferation rate result in motion arrest at higher shape parameters. Moreover, CDK1 inhibition immediately abrogates movement and further epithelial remodeling. While previous data has implicated the importance of mitotic rounding

as a source of stress (37, 64, 65), we do not observe large local distortions (*SI Appendix*, Fig. S11). Therefore, we have demonstrated a role for an active stress generated during interphase or potentially through non–cell autonomous behaviors. Cell cycle–dependent processes which impact cell adhesion (53), junction tension, and cortical mechanics (54, 66) all could give rise to the active stress generation during interphase. Disentangling these effects will be an interesting avenue for future research on cell shape remodeling in epithelia.

Cell proliferation rates can vary widely across different tissues (e.g., the intestine can be entirely replaced on the timescale of days to weeks while the skin may turn over on the timescale of months) (67). Moreover, epithelial turnover can be upregulated in response to external stimuli and tissue damage (68–70). Regulation of cell division rates under these different circumstances may be a way for the epithelium to tune fluidity and facilitate repair. The extent to which the cell turnover rate is used to regulate epithelial fluidity and architecture in vivo will be an interesting line of future research. Numerous recent studies have identified a role for cell division in driving morphogenetic processes (13, 64, 71, 72). Our data suggest a mechanism for the increased fluidity observed in highly proliferative tissues through an increase in active stress generation. Measurements of cell shape and motility in these different contexts are required to determine if they are similarly driven by cell cycle–dependent active stress and to discover new mechanisms driving epithelial organization. Further understanding of the interplay between cell cycle, tissue mechanics, and cell shape remodeling may lead to a more comprehensive understanding of tissue function in development, homeostasis, and disease.

Materials and Methods

MDCK cells were cultured under standard conditions in Dulbecco's Modified Eagle's Medium (DMEM) with 10% fetal bovine serum (FBS) at 37°C and 5% CO₂. Cell monolayers were prepared on by seeding $\sim 6 \times 10^5$ MDCK cells on a 500-mm² collagen gel substrate overnight. Collagen gels were prepared by polymerizing a neutral collagen solution on silane–glutaraldehyde modified glass substrates for 1 h. Cells were imaged by widefield fluorescence microscopy using standard filter sets. We imaged many locations in the monolayer and verified that they show qualitatively similar behavior (*SI Appendix*, Fig. S15) Image segmentation, cell tracking, and cell division detection were done using custom MATLAB code based on previous methods (73, 74). An example of this segmentation can be seen in the supplement (*Movie S8*). By tracking fixed monolayers, we found that the tracking errors are small compared to cell motions (*SI Appendix*, Fig. S16). We also found that stage drift is sufficiently small to be corrected for drift by subtracting the mean displacement. Simulations of the thermal Voronoi model were performed as described in previous publications (43, 44). A detailed description of all methods can be found in *SI Appendix*.

Data Availability. Plasmids from this study will be made available from the corresponding authors upon reasonable request and through Addgene (<https://www.addgene.org>). Code will be made available on the GitHub (<https://github.com/sussmanLab/cellGPU>, <https://github.com/GardellLab/MonolayerTracking>). Image data and cell trajectories are available on Figshare [<https://doi.org/10.6084/m9.figshare.14043848.v2> (75)].

ACKNOWLEDGMENTS. M.L.G. acknowledges funding from NIH RO1 GM104032 and Army Research Office Multidisciplinary University Research Initiative W911NF1410403. M.L.M. acknowledges funding from a Simons Foundation Collaboration grant on Cracking the Glass Problem (#454947) and in the Mathematical Modeling of Living Systems (#446222) as well as NSF-PHY-1607416. T.Y. acknowledges KAKENHI Grant No. 19K16096 and Research Grant from Human Frontier Science Program (Ref. Grant No. RGY0081/2019). This project was initiated by Scialog Funding awarded to M.L.G. and M.L.M.

1. M. J. Bissell, A. Rizki, I. S. Mian, Tissue architecture: The ultimate regulator of breast epithelial function. *Curr. Opin. Cell Biol.* **15**, 753–762 (2003).
2. T. P. J. Wyatt *et al.*, Emergence of homeostatic epithelial packing and stress dissipation through divisions oriented along the long cell axis. *Proc. Natl. Acad. Sci. U.S.A.* **112**, 5726–5731 (2015).

3. H. Honda, Y. Ogita, S. Higuchi, K. Kani, Cell movements in a living mammalian tissue: Long-term observation of individual cells in wounded corneal endothelia of cats. *J. Morphol.* **174**, 25–39 (1982).
4. M. Takeichi, Dynamic contacts: Rearranging adherens junctions to drive epithelial remodelling. *Nat. Rev. Mol. Cell Biol.* **15**, 397–410 (2014).

5. J.-A. Park *et al.*, Unjamming and cell shape in the asthmatic airway epithelium. *Nat. Mater.* **14**, 1040–1048 (2015).
6. C. Luxenburg, R. Zaidel-Bar, From cell shape to cell fate via the cytoskeleton—Insights from the epidermis. *Exp. Cell Res.* **378**, 232–237 (2019).
7. F. Bosveld *et al.*, Epithelial tricellular junctions act as interphase cell shape sensors to orient mitosis. *Nature* **530**, 495–498 (2016).
8. R. Farhadifar, J.-C. Röper, B. Aigouy, S. Eaton, F. Jülicher, The influence of cell mechanics, cell-cell interactions, and proliferation on epithelial packing. *Curr. Biol.* **17**, 2095–2104 (2007).
9. M. C. Gibson, A. B. Patel, R. Nagpal, N. Perrimon, The emergence of geometric order in proliferating metazoan epithelia. *Nature* **442**, 1038–1041 (2006).
10. B. Dubretret, N. Rivier, The renewal of the epidermis: A topological mechanism. *Biophys. J.* **73**, 38–44 (1997).
11. R. David *et al.*, Tissue cohesion and the mechanics of cell rearrangement. *Development* **141**, 3672–3682 (2014).
12. A. Mongera *et al.*, A fluid-to-solid jamming transition underlies vertebrate body axis elongation. *Nature* **561**, 401–405 (2018).
13. J. Firmino, D. Rocancourt, M. Saadaoui, C. Moreau, J. Gros, Cell division drives epithelial cell rearrangements during gastrulation in chick. *Dev. Cell* **36**, 249–261 (2016).
14. T. Lecuit, P.-F. Lenne, Cell surface mechanics and the control of cell shape, tissue patterns and morphogenesis. *Nat. Rev. Mol. Cell Biol.* **8**, 633–644 (2007).
15. S. Alt, P. Ganguly, G. Salbreux, Vertex models: From cell mechanics to tissue morphogenesis. *Philos. Trans. R Soc. Lond. B Biol. Sci.* **372**, 20150520 (2017).
16. E. Marinari *et al.*, Live-cell delamination counterbalances epithelial growth to limit tissue overcrowding. *Nature* **484**, 542–545 (2012).
17. D. B. Staple *et al.*, Mechanics and remodelling of cell packings in epithelia. *Eur. Phys. J. E Soft Matter* **33**, 117–127 (2010).
18. H. Honda, G. Eguchi, How much does the cell boundary contract in a monolayered cell sheet? *J. Theor. Biol.* **84**, 575–588 (1980).
19. D. Bi, X. Yang, M. C. Marchetti, M. L. Manning, Motility-driven glass and jamming transitions in biological tissues. *Phys. Rev. X* **6**, 021011 (2016).
20. A. Haeger, M. Krause, K. Wolf, P. Friedl, Cell jamming: Collective invasion of mesenchymal tumor cells imposed by tissue confinement. *Biochim. Biophys. Acta* **1840**, 2386–2395 (2014).
21. L. Oswald, S. Grosser, D. M. Smith, J. A. Käs, Jamming transitions in cancer. *J. Phys. D Appl. Phys.* **50**, 483001 (2017).
22. J. Ranft *et al.*, Fluidization of tissues by cell division and apoptosis. *Proc. Natl. Acad. Sci. U.S.A.* **107**, 20863–20868 (2010).
23. S. Henkes, Y. Fily, M. C. Marchetti, Active jamming: Self-propelled soft particles at high density. *Phys. Rev. E Stat. Nonlin. Soft Matter Phys.* **84**, 040301 (2011).
24. X. Yang *et al.*, Correlating cell shape and cellular stress in motile confluent tissues. *Proc. Natl. Acad. Sci. U.S.A.* **114**, 12663–12668 (2017).
25. D. Bi, J. H. Lopez, J. M. Schwarz, M. L. Manning, A density-independent rigidity transition in biological tissues. *Nat. Phys.* **11**, 1074–1079 (2015).
26. S. Kim, S. Hilgenfeldt, Cell shapes and patterns as quantitative indicators of tissue stress in the plant epidermis. *Soft Matter* **11**, 7270–7275 (2015).
27. T. Lecuit, P.-F. Lenne, E. Munro, Force generation, transmission, and integration during cell and tissue morphogenesis. *Annu. Rev. Cell Dev. Biol.* **27**, 157–184 (2011).
28. N. S. Rossen, J. M. Tarp, J. Mathiesen, M. H. Jensen, L. B. Oddershede, Long-range ordered vorticity patterns in living tissue induced by cell division. *Nat. Commun.* **5**, 5720 (2014).
29. O. Chepizhko *et al.*, Bursts of activity in collective cell migration. *Proc. Natl. Acad. Sci. U.S.A.* **113**, 11408–11413 (2016).
30. T. E. Angelini *et al.*, Glass-like dynamics of collective cell migration. *Proc. Natl. Acad. Sci. U.S.A.* **108**, 4714–4719 (2011).
31. S. Garcia *et al.*, Physics of active jamming during collective cellular motion in a monolayer. *Proc. Natl. Acad. Sci. U.S.A.* **112**, 15314–15319 (2015).
32. L. Atia *et al.*, Geometric constraints during epithelial jamming. *Nat. Phys.* **14**, 613–620 (2018).
33. C. Malinverno *et al.*, Endocytic reawakening of motility in jammed epithelia. *Nat. Mater.* **16**, 587–596 (2017).
34. A. Puliafito *et al.*, Collective and single cell behavior in epithelial contact inhibition. *Proc. Natl. Acad. Sci. U.S.A.* **109**, 739–744 (2012).
35. S. Kim, M. Pochitaloff, O. Campàs, G. Stooke-Vaughan, Embryonic tissues as active foams. *bioRxiv* [Preprint] (2020). <https://doi.org/10.1101/2020.06.17.157909> (Accessed 17 February 2021).
36. A. I. McClatchey, A. S. Yap, Contact inhibition (of proliferation) redux. *Curr. Opin. Cell Biol.* **24**, 685–694 (2012).
37. A. Doostmohammadi *et al.*, Celebrating soft matter's 10th anniversary: Cell division: A source of active stress in cellular monolayers. *Soft Matter* **11**, 7328–7336 (2015).
38. D. A. Matoz-Fernandez, K. Martens, R. Sknepnek, J. L. Barrat, S. Henkes, Cell division and death inhibit glassy behaviour of confluent tissues. *Soft Matter* **13**, 3205–3212 (2017).
39. M. Czajkowski, D. M. Sussman, M. C. Marchetti, M. L. Manning, Glassy dynamics in models of confluent tissue with mitosis and Apoptosis. *Soft Matter* **15**, 9133–9149 (2019).
40. M. R. Ng, A. Besser, G. Danuser, J. S. Brugge, Substrate stiffness regulates cadherin-dependent collective migration through myosin-II contractility. *J. Cell Biol.* **199**, 545–563 (2012).
41. X. Trepat *et al.*, Physical forces during collective cell migration. *Nat. Phys.* **5**, 426–430 (2009).
42. C. De Pascalis *et al.*, Intermediate filaments control collective migration by restricting traction forces and sustaining cell-cell contacts. *J. Cell Biol.* **217**, 3031–3044 (2018).
43. D. M. Sussman, cellGPU: Massively parallel simulations of dynamic vertex models. *Comput. Phys. Commun.* **219**, 400–406 (2017).
44. D. M. Sussman, M. Paoluzzi, M. Cristina Marchetti, M. Lisa Manning, Anomalous glassy dynamics in simple models of dense biological tissue. *EPL* **121**, 36001 (2018).
45. L. Yan, D. Bi, Multicellular rosettes drive fluid-solid transition in epithelial tissues. *Phys. Rev. X* **9**, 011029 (2019).
46. X. Wang *et al.*, Anisotropy links cell shapes to tissue flow during convergent extension. *Proc. Natl. Acad. Sci. U.S.A.* **117**, 13541–13551 (2020).
47. S. van Helvert, C. Storm, P. Friedl, Mechanoreciprocity in cell migration. *Nat. Cell Biol.* **20**, 8–20 (2018).
48. L. H. H. Olde Damink *et al.*, Glutaraldehyde as a crosslinking agent for collagen-based biomaterials. *J. Mater. Sci. Mater. Med.* **6**, 460–472 (1995).
49. N. R. Lang *et al.*, Biphasic response of cell invasion to matrix stiffness in three-dimensional biopolymer networks. *Acta Biomater.* **13**, 61–67 (2015).
50. Z. Tang *et al.*, Mechanical forces program the orientation of cell division during airway tube morphogenesis. *Dev. Cell* **44**, 313–325.e5 (2018).
51. C. Collinet, M. Rauzi, P.-F. Lenne, T. Lecuit, Local and tissue-scale forces drive oriented junction growth during tissue extension. *Nat. Cell Biol.* **17**, 1247–1258 (2015).
52. K. E. Cavanaugh, M. F. Staddon, E. Munro, S. Banerjee, M. L. Gardel, RhoA mediates epithelial cell shape changes via mechanosensitive endocytosis. *Dev. Cell* **52**, 152–166.e5 (2020).
53. M. C. Jones, J. A. Askari, J. D. Humphries, M. J. Humphries, Cell adhesion is regulated by CDK1 during the cell cycle. *J. Cell Biol.* **217**, 3203–3218 (2018).
54. B. Vianay *et al.*, Variation in traction forces during cell cycle progression. *Biol. Cell* **110**, 91–96 (2018).
55. J.-L. Maître *et al.*, Adhesion functions in cell sorting by mechanically coupling the cortices of adhering cells. *Science* **338**, 253–256 (2012).
56. A.-A. Chassot *et al.*, Confluence-induced cell cycle exit involves pre-mitotic CDK inhibition by p27(Kip1) and cyclin D1 downregulation. *Cell Cycle* **7**, 2038–2046 (2008).
57. S. R. Podmirsej *et al.*, Caspases uncouple p27(Kip1) from cell cycle regulated degradation and abolish its ability to stimulate cell migration and invasion. *Oncogene* **35**, 4580–4590 (2016).
58. A. Besson, M. Gurian-West, A. Schmidt, A. Hall, J. M. Roberts, p27Kip1 modulates cell migration through the regulation of RhoA activation. *Genes Dev.* **18**, 862–876 (2004).
59. T. Yamamoto, D. M. Sussman, T. Shibata, M. L. Manning, Non-monotonic fluidization generated by fluctuating edge tensions in confluent tissues. *arXiv* [Preprint] (2020). 2008.13007 (Accessed 17 February 2021).
60. G. D. Grant, K. M. Kedziora, J. C. Limas, J. G. Cook, J. E. Purvis, Accurate delineation of cell cycle phase transitions in living cells with PIP-FUCCI. *Cell Cycle* **17**, 2496–2516 (2018).
61. S. J. Streichan, C. R. Hoerner, T. Schneidt, D. Holzer, L. Hufnagel, Spatial constraints control cell proliferation in tissues. *Proc. Natl. Acad. Sci. U.S.A.* **111**, 5586–5591 (2014).
62. G. Charras, A. S. Yap, Tensile forces and mechanotransduction at cell-cell junctions. *Curr. Biol.* **28**, R445–R457 (2018).
63. A. Munjal, J.-M. Philippe, E. Munro, T. Lecuit, A self-organized biomechanical network drives shape changes during tissue morphogenesis. *Nature* **524**, 351–355 (2015).
64. N. I. Petridou, S. Grigolon, G. Salbreux, E. Hannezo, C.-P. Heisenberg, Fluidization-mediated tissue spreading by mitotic cell rounding and non-canonical Wnt signalling. *Nat. Cell Biol.* **21**, 169–178 (2019).
65. S. P. Ramanathan *et al.*, Cdk1-dependent mitotic enrichment of cortical myosin II promotes cell rounding against confinement. *Nat. Cell Biol.* **17**, 148–159 (2015).
66. P. Chugh *et al.*, Actin cortex architecture regulates cell surface tension. *Nat. Cell Biol.* **19**, 689–697 (2017).
67. C. E. S. Hooper, Cell turnover in epithelial populations. *J. Histochem. Cytochem.* **4**, 531–540 (1956).
68. J. Liang, S. Balachandra, S. Ngo, L. E. O'Brien, Feedback regulation of steady-state epithelial turnover and organ size. *Nature* **548**, 588–591 (2017).
69. S. A. Gudipaty *et al.*, Mechanical stretch triggers rapid epithelial cell division through Piezo1. *Nature* **543**, 118–121 (2017).
70. H. Pinkus, Examination of the epidermis by the strip method of removing horny layers. I. Observations on thickness of the horny layer, and on mitotic activity after stripping. *J. Invest. Dermatol.* **16**, 383–386 (1951).
71. M. Saadaoui, D. Rocancourt, J. Roussel, F. Corson, J. Gros, A tensile ring drives tissue flows to shape the gastrulating amniote embryo. *Science* **367**, 453–458 (2020).
72. B. G. Godard, C.-P. Heisenberg, Cell division and tissue mechanics. *Curr. Opin. Cell Biol.* **60**, 114–120 (2019).
73. J. C. Crocker, D. G. Grier, Methods of digital video microscopy for colloidal studies. *J. Colloid Interface Sci.* **179**, 298–310 (1996).
74. M. H. Asghari, B. Jalali, Edge detection in digital images using dispersive phase stretch transform. *Int. J. Biomed. Imaging* **2015**, 687819 (2015).
75. J. Devany, M. L. Gardel, Cell division rate controls cell shape remodeling in epithelia - imaging and tracking data. *Figshare*. <https://doi.org/10.6084/m9.figshare.14043848.v2>. Deposited 18 February 2021.